Discrete superstructures in low-resolution images

Siarhei Khirevich[a)] and Tadeusz W. Patzek

Ali I. Al-Naimi Petroleum Engineering Research Center,

King Abdullah University of Science and Technology, Thuwal,

Saudi Arabia

(Dated: 17 March 2025)

Flow through porous media occurs in everyday life, including scientific, medical, and engineering applications. Realistic pore-scale simulations of flow frequently use discrete images (pixels in two dimensions or voxels in three dimensions) of real-life samples as inputs. Today's commonly held belief is that higher-accuracy simulations require higher-resolution images, which often result in lengthy scanning and/or simulation times. Conversely, decreasing the resolution destroys the simulation accuracy when the features of the sample (e.g., pores) are unresolved. Here, we report the discovery of superstructures in discrete images, which emerge from the sample's features and discrete mesh. These superstructures — and not the original features of the sample — control flow in low-resolution simulations. Consequently, decreases in resolution change the topology (flow "pathways") and morphology (pore "shapes") in the discrete image of the sample. Using permeability as an example, we present a new methodology to enhance the flow simulation accuracy for both low resolution X-ray Computed Tomography-imaged and computer-generated samples. This methodology is based on the novel concept of "null point", P0, and voxel-based resolution parameter, χ. The presented methodology improves extraction of quantitative information from discrete images. Our findings are not limited by image dimensionality, imaging technique, or simulated processes.

[a)]Electronic mail: khirevich@gmail.com

I. INTRODUCTION

Computer simulations can serve as powerful tools to understand and predict real-life results only when they accurately mimic experiments. In particular, simulations of fluid flow in complex geometries are highly relevant to a variety of scientific and industrial applications[1–14]. Computer simulations originating from first principles (based on the solutions of partial differential equations (PDEs) such as the Navier–Stokes equation for fluid flow) can be used to verify laboratory results, and guide experiments[15]. The complexity of real-life problems requires the solution of PDEs to be numerical, which in most cases necessitates the use of discrete meshes. The basic uniform Cartesian mesh is not only involved in the solutions of PDEs, but is also routinely found in the imaging of real-life objects in the form of pixels or voxels. For example, two-dimensional digital photography produces a set of pixels while three-dimensional X-ray, magnetic, or optical scanning produces a set of voxels.

The finite memory of digital computers limits the number of mesh elements (e.g., pixels) in an image, and it seems that an optimal approach to image an arbitrary-shaped object is to distribute the mesh elements in space uniformly along Cartesian directions. This approach generates pixels in two dimensions or voxels in three dimensions. However, mapping real-life objects or processes onto a Cartesian mesh unavoidably leads to the discretization error. In the context of flow simulations, the discretization error impacts both the geometry representation and the flow field, with the latter originating from the numerical solution of PDEs. As the result, this discretization error contaminates the physics of flow simulations. Minimization of the discretization error is required to validate the computer models, and ensure they accurately reproduce the experiment. Refining the mesh (increasing the resolution) is an option; however, this route leads to prohibitive scanning and/or simulation times. Therefore, obtaining a smaller discretization error at lower resolutions is of utmost practical importance.

Previous research on pore-scale flow simulations has reported[7,16–18] improving flow simulation accuracy via i) the addition of detailed information about each pore (i.e., a solid boundary between mesh nodes), and/or ii) pores of the sample to be sufficiently resolved by the mesh. Low-resolution images with unresolved pores are naturally avoided for accurate flow simulations. Low resolution Computed Tomography (CT)-scanned images are also impacted by the fundamental limitation of image contrast, which further complicates

the entire process of obtaining accurate geometry followed by flow simulations[15,19]. In this study, we deal with the packings of closely-packed spheres discretized on a uniform cubic mesh. We refer to the discretization resolutions of below $\sim$10 voxels per sphere diameter as "low", while resolutions of above $\sim$50 voxels per sphere diameter are considered as "high". If we consider the hydraulic diameter d_{h} to be about one third of a sphere diameter for a packing with porosity of 0.35[20,21], then the low resolutions will correspond to $d_{\mathrm{h}} \lesssim 3$ voxels while high resolutions to $d_{\mathrm{h}} \gtrsim 15$.

Here, we analyze and aim to minimize the discretization error in simulations of flow through a porous sample, providing the new physical insights into flow simulations. The pore-scale flow simulations are highly sensitive to the topology (flow "pathways") and morphology (pore "shapes") of the pore space. In this study, we 1) apply fractional discretization and visualize superstructures, which can be visible when regular sphere packings are mapped onto the discrete mesh at low resolutions, 2) simulate flow to obtain permeability of a porous sample, 3) establish similarity in the permeability error between regular and irregular geometries, 4) vary the free adjustable parameter of the lattice Boltzmann flow solver, which controls the discretization errors ("magic number"), 5) highlight the existence of the "null point", where low-resolution flow field provides accurate permeability value due to self-cancellation of the discretization error contributions, and 6) propose a linear correlation between the geometrical parameter χ and the magic number. Finally, we demonstrate the presented linear correlation leads to an excellent error reduction of the permeabilities computed from the three-dimensional (3D) images of laboratory-prepared samples relative to the experimentally measured values[15].

II. FRACTIONAL DISCRETIZATION AND SUPERSTRUCTURES

Conventional pore-scale flow simulations require discretization of a porous sample by mapping it onto a cubic mesh and marking each mesh voxel as either `solid` or `fluid` based on its center location relative to the sample solid phase (Figure 1B). The ratio (number of `fluid` voxels)/(total number of voxels) defines the discrete porosity. We initially define the discretization resolution as the number of voxels per sphere diameter. For regular geometries and low discretization resolutions, we maintain the discrete porosity of each geometry close to its analytical value with minor adjustments of the sphere radii during discretization, if

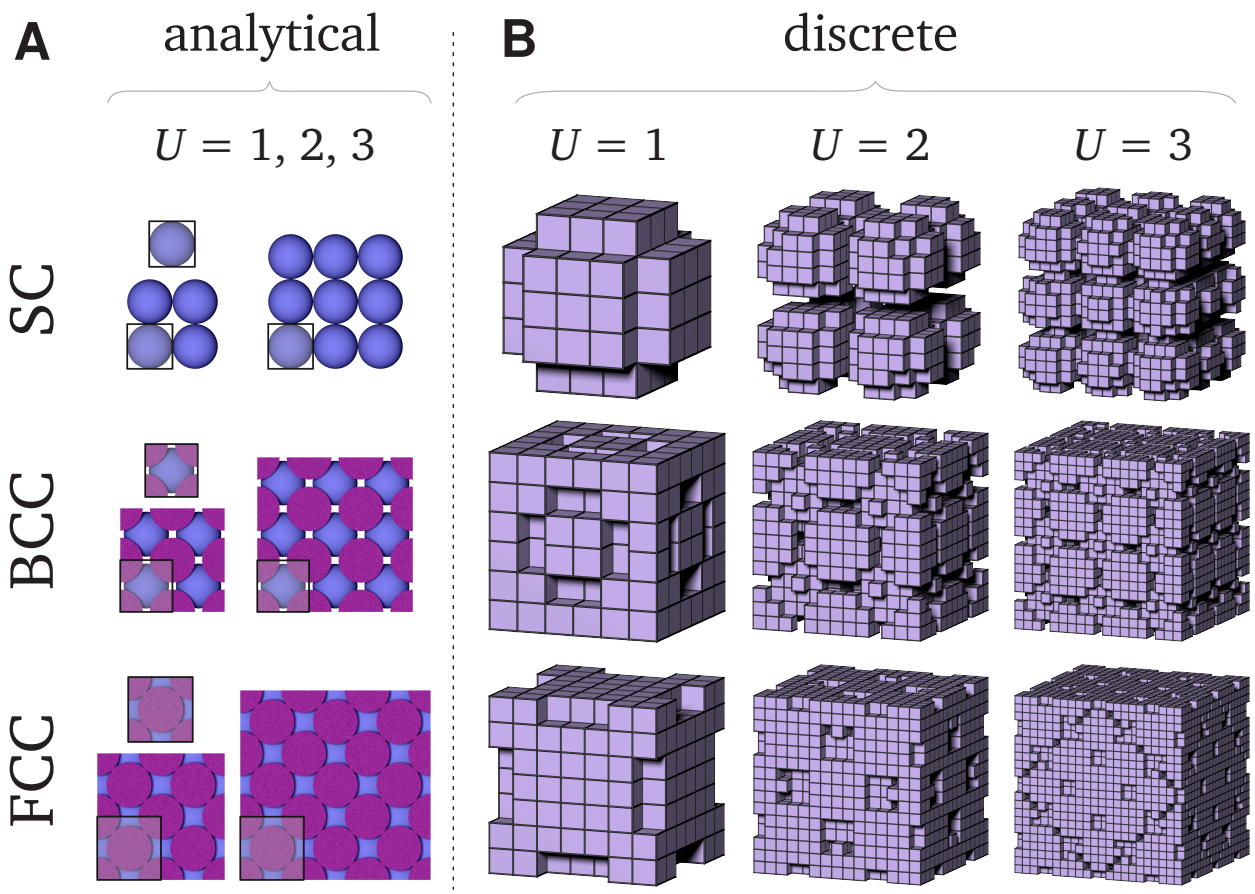

FIG. 1. Analytical (A) and discrete (B) representations of SC, BCC, and FCC packings of touching spheres. Gray boxes indicate a single unit cell. B: Each geometry is discretized at the resolution of about 5 voxels/sphere diameter; left column shows integer L/U ratios, while the middle and right columns depict non-integer L/U ratios. For SC geometry, $L/U = 5/1 = 5$ in the left column while $L/U = 11/5$ and $L/U = 16/3$ in the middle and right columns, resulting in the simulation domain dimensions of 5^3, 11^3, and 16^3, respectively. The superstructures appear in columns $U = 2$ and $U = 3$ as geometric structures with dimensions exceeding one unit cell.

there is a noticeable difference between analytical and discrete porosities.

To visualize the discrete meshes originating from regular geometries, we consider the smallest case of a porous sample to be a single sphere. When coupled with periodic boundary conditions, this geometry results in a simple cubic (SC) packing with an analytical porosity of $1 - \pi/6 \approx 0.476$ (Figure 1A, top row). The selected flow simulation approach requires an integer number of nodes (L) per each dimension of the simulation domain. We use the periodicity property and replicate the SC unit cell U times along each Cartesian

direction. When the ratio L/U is non-integer, each cubic unit cell has a non-integer number of mesh nodes per edge, while L always remains an integer. We refer to this process as the fractional discretization procedure[22]. The top row of Figure 1B illustrates that the fractional discretization procedure results in feature-rich voxelized geometries ($U = 2$, $U = 3$) compared to the geometries of similar resolution with an integer L/U ratio ($U = 1$). Note that increasing U alone adds no new information to the analytical geometry — it is a simple replication of SC unit cell. An identical outcome is observed for both body- and face-centered cubic packings (BCC and FCC), as seen in the middle and bottom rows in Figure 1. These results show that the fractional discretization results in superstructures — structures with dimensions that significantly exceed one unit cell.

III. SIMILARITY IN NUMERICAL ERROR IN PERMEABILITY

To assess the accuracy of flow simulations, we focus on the permeability, calculated using the average velocity in the direction of the applied pressure gradient. (Permeability quantifies the capacity of a given geometry with voids to conduct a fluid.) The simulated flow is single-phase and pressure-driven, and occurs in the voids of geometries formed by the closely-packed spheres at various void space fractions (porosities). We simulate a zero-Reynolds number flow which obeys Stokes PDE, with solutions obtained using the two-relaxation-time lattice Boltzmann method (LBM)[23] implemented as described in[24]. The no-slip boundary condition is enforced using the bounce-back rule. Applied pressure drop and the corresponding macroscopic flow are directed along one of the principal axes. We perform flow simulations in the void space of SC and irregular (containing 14400 spheres, Figure 2 inset) geometries of identical porosities, and calculate the permeability error relative to a reference value. Both SC and irregular geometries have their own $\sim$0.1%-accurate reference permeability values k_{ref} obtained using extrapolation[24], see Tables I and II for the complete list of values. These reference values can be obtained in different ways, for example pushing resolutions to prohibitive levels such as $\sim 10^3$–10^4 voxels/sphere diameter, replacing bounce back with higher-order boundary conditions and using moderate resolutions of $\sim 10^2$, or using any non-LBM numerical scheme which will provide resolution-free permeability values based on the solution of Stokes equation.

Figure 2 compares variation of the relative error in permeability vs. resolution for the

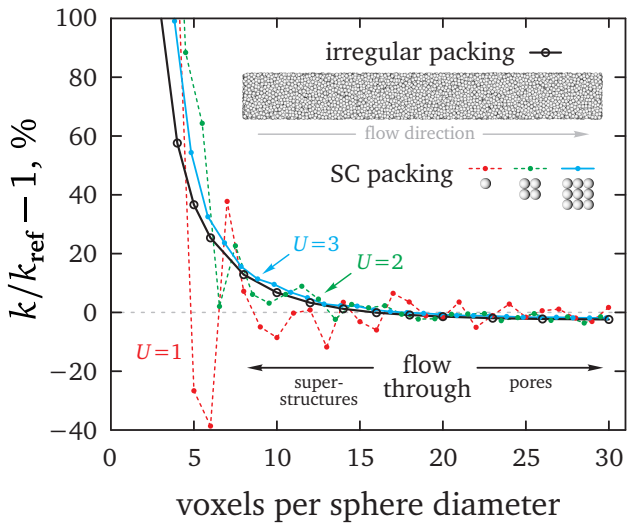

FIG. 2. Relative error in permeability vs. discretization resolution. Red, green, and blue dots depict SC packing with an increasing number of unit cell replications along each Cartesian direction (U). Black circles refer to an irregular packing with the size of $12 \times 12 \times 100$ sphere diameters depicted in the inset. Both geometries have the identical porosity of $1-\pi/6 \approx 0.476$. The reference permeability values (i.e., the gray dashed line) are different for SC and irregular packings, and are provided in Tables I and II.

SC and irregular geometries. This figure demonstrates that increasing the number of unit cells per domain edge U, while preserving a non-integer L/U ratio, reduces the scatter of the relative error in permeability for the SC geometry. Also, with the increase of U, the relative error for the SC geometry begins to follow the irregular one. This means that when a superstructure within the SC geometry reaches a sufficient size, the SC geometry displays the resolution–permeability error dependency similar to the irregular geometry. This finding suggests the existence of superstructures in not only regular but also in irregular geometries.

To visualize the impact of superstructures on the flow field for the SC geometry, we color each `fluid` voxel according to its absolute velocity magnitude. To reveal the skeleton of the flow field, Figure 3 shows about 200 voxels with the highest magnitude. The skeleton in Figure 3 resembles the features of the superstructures shown in Figure 1B. Figure 3 reveals that 1) similar to the superstructures seen in Figure 1B, the size of each flow field skeleton also significantly exceeds one unit cell, and 2) the skeleton (and superstructures) do not resemble the pore space of the underlying analytical geometry. The first point suggests that construction of any scheme to numerically solve Stokes PDE inside a unit cell cannot

capture the entire superstructure because of insufficient information on the pore space. For the considered flow problem we are not aware of any numerical scheme constructed outside of a unit cell: the numerical schemes such as the lattice Boltzmann and finite difference rely on the information from a given voxel plus its direct neighbors, which is below the unit cell scale. The second point demonstrates that the superstructures — *not pores* — control flow at low resolutions, and implies that varying the resolution changes both morphology and topology of the voxelized pore space. Conversely, with increasing resolution from low to high values, the impact of superstructures disappear and flow occurs through the pores of the underlying analytical geometry (see Figure 8 as an example for SC geometry).

We note that visualization of the flow skeleton and the corresponding superstructures for irregular geometries will be limited as any observed local velocity maxima (which form the superstructures in Figure 3) can be attributed to a slightly larger pore sampled by a given voxel. But, similarities in the resolution–error curves in Figure 2 suggest that irregular geometries also contain the superstructures.

IV. MAGIC NUMBER, Λ.

The discretization error is the key artifact separating computer simulations from their real-life counterparts. A *free* parameter known as the "magic number", Λ, controls the spatial discretization error in two-relaxation-times lattice Boltzmann simulations[23,25]. In this section, we provide essential background details on Λ. In later sections of this study, Λ together with geometrical parameter χ will be used to construct a universal correlation which significantly reduces the discretization error in permeability simulations.

LBM simulates the fluid with fictitious particles that occupy the discrete mesh and propagate along the prescribed discrete links at discrete time steps. On each iteration, the particles collide at mesh nodes according to a predefined collision operator. The collision operator can be formulated differently[26–28], but it always includes at least one collision (relaxation) rate. In the basic case of Stokes flow and the collision operator with a single rate, this rate controls both viscosity of the simulated fluid and the spatial discretization error[26]. The adjustment of viscosity separately from the discretization error can be done with at least two collision rates, which resulted in the formulation of two-relaxation-times (TRT) collision operator[23]. Then Λ is a specific combination of the LBM collision rates[25].

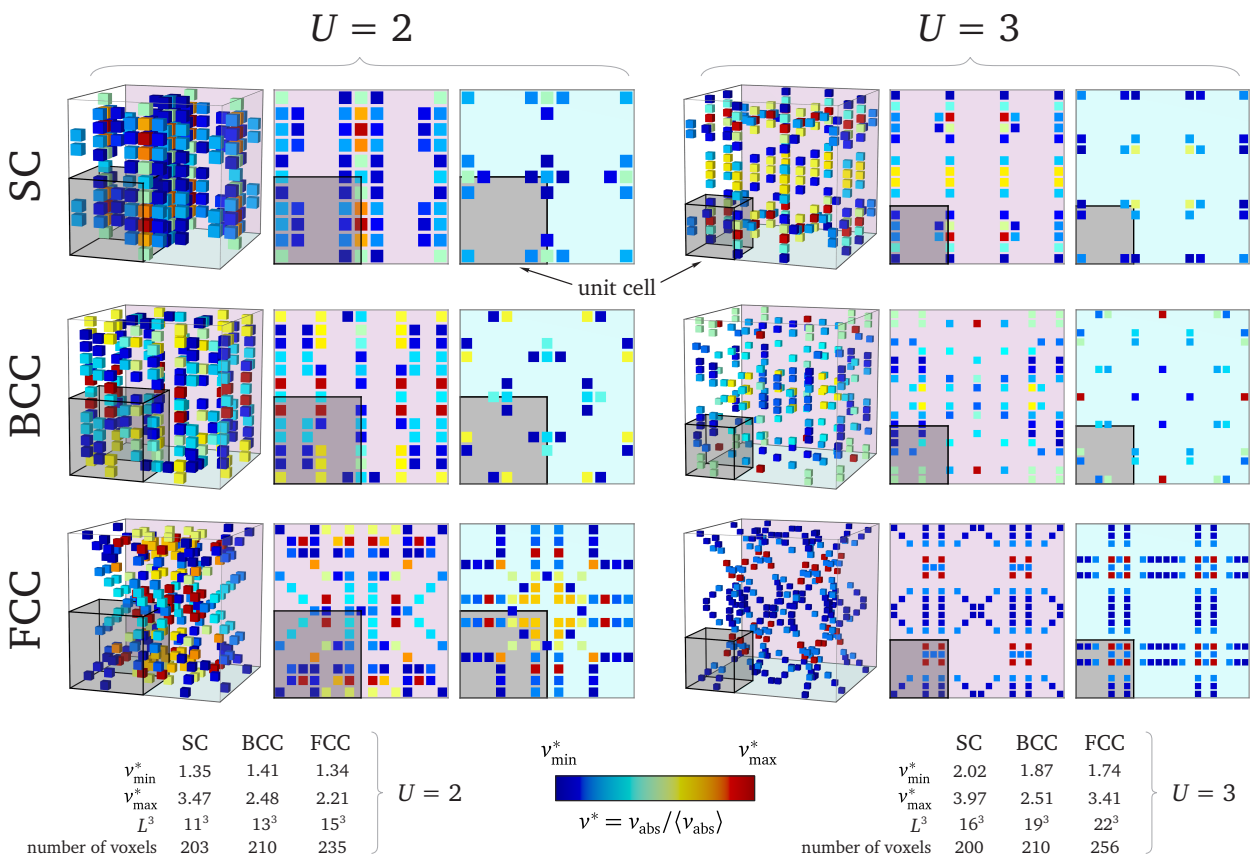

FIG. 3. Each panel displays approximately 200 voxels with the highest absolute velocity magnitude extracted from the full velocity field. Each column shows perspective, front, and top views for the SC, BCC, and FCC geometries of touching spheres with $U = 2$ and $U = 3$. Discretization resolution is about 5.3 voxels per sphere diameter for all geometries. The gray-shaded cube depicts the unit cell corresponding to each geometry. Colorbar limits, simulation domain dimensions, and the number of voxels shown for each packing type and U are provided at the bottom. Light blue and red faces in perspective view help to identify the corresponding top and front views. All discrete geometries have reflection symmetry for all Cartesian axes also seen in the velocity fields. Additional cases of $U = 4$ and $U = 5$ are shown in Figure 6. We do not show $U = 1$ geometries because the flow field dimensions are limited to a single unit cell.

Note that not all collision operators with two rates separate the viscosity control from the discretization error (see section 2.1.3 in[22]). For the collision operators with multiple rates[27], several combinations of the collision rates needs to be fixed to separate viscosity adjustment from the spatial discretization errors, see discussion in sections 2.1.4, 2.2.3 in[22].

The collision operator defines the numerical scheme in the bulk, away from the `solid`–

`fluid` interface, while the boundary condition completes the scheme at the interface. The continuum description of flow around a solid obstacle assumes zero-flow velocity at the solid boundary which is also known as the no-slip boundary condition. To implement this boundary condition at the `solid`–`fluid` interface in voxelized images, we use the popular "bounce-back" LBM boundary condition[29]. Λ can be seen as the parameter controlling i) the location of the zero-flow boundary (and the corresponding pore "width") between `solid` and `fluid` voxels[22], or ii) the magnitude of the discretization error or its contributions (see Figure 3 in[24]; also eq. (15) in[30], where parameter τ can be interpreted as the one impacting the discretization error).

The existence of the free parameter Λ requires it to be assigned a value before running a simulation, as there is no clear guidance for a particular choice of Λ for simulations in complex geometries. The numerical permeability obtained with LBM and the bounce-back rule for a given geometry is arbitrary, and it is controlled by Λ[22,25], although the impact of Λ on the permeability decreases with the mesh refinement. If we consider popular reformulations of the collision operator, such as the Bhatnagar–Gross–Krook operator-based[26] (BGK), multiple-relaxation-times[27,31], or cumulant-based[28] (e. g., eq. (12) in[32]), the free choice of Λ impacts all of them. That is, the choice of Λ is of fundamental importance to obtain accurate simulation results.

Currently, a robust theoretical analysis for the simple system of flow between two parallel plates suggests taking $\Lambda = 3/16$ (or $3/8$) for the exact flow field at *any* discretization resolution in a horizontal (or 45°-inclined) channel relative to the underlying mesh[22,33]. Similarly, $\Lambda = 1/8$ provides the exact average velocity, canceling the velocity integration error[34]. Figure 4A adds the impact of Λ to the results from Figure 2, showing the error in permeability vs. resolution at different values of Λ. Figure 4A also shows that once the geometry includes curved boundaries, these Λ values no longer result in the most accurate permeability[22]. Note that in Figure 4A increase of the resolution from low to high result in all curves converging to zero from above, crossing the zero error value, and then slowly continuing to converge up from below. (This also includes $\Lambda = 3/8$ in Figure 4A, as can be seen in Figure 8c,d in[22].) This is counterintuitive because increases in resolution may result in larger permeability errors.

The impact of Λ on simulated permeability can be significantly reduced[18,22] after replacing the first-order bounce-back boundary condition with a higher-order one. This replacement

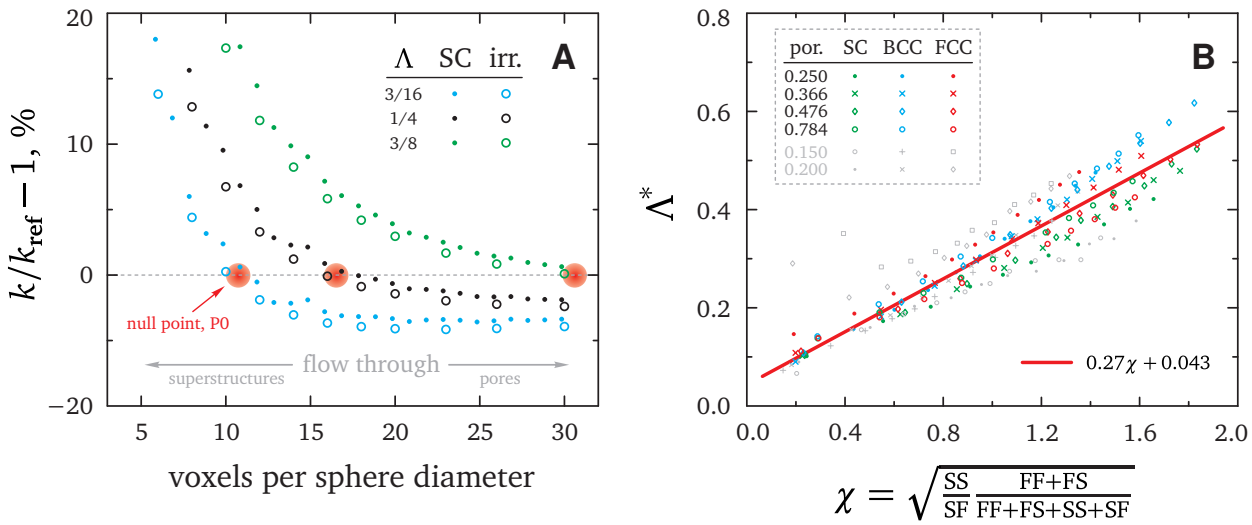

FIG. 4. A: Relative error in permeability vs. discretization resolution for irregular (circles) and SC (dots) packings with the porosity of about 0.476. Each large red circle indicates the "null point", P0, for a given Λ. B: Λ^* vs. the dimensionless parameter χ for the SC, BCC, FCC packings with the porosities of 0.25, 0.366, 0.476, 0.784 each. Additional porosities of 0.15 and 0.2 (gray symbols) are only for completeness and are not used in the linear fit.

is only possible after adding information on the location of the pore boundaries between the mesh nodes to the LBM simulations. However, this approach has fundamental limitations when recovering pore surfaces from real voxelized images. Namely, i) recovery of a surface using, e.g., the marching cubes algorithm[35] does not converge to the analytical result even in the case of a single sphere[36]; and ii) during imaging, contrast loss occurs non-uniformly within each pore[15], which prevents pore surface recovery from the intensity of each voxel.

V. NULL POINT, P0, AND PARAMETER χ.

Each curve in Figure 4A demonstrates a distinct point which we call the "null point" or P0. At P0, the resolution can be low (unresolved geometry and flow field), the error in permeability is small ($\sim$1%), and any resolution deviation from P0 increases the error magnitude. This small error at P0 originates from the self-cancellation of three components of the discretization error: the LBM scheme away from the `solid`–`fluid` interface, the boundary condition, and the integration while calculating the average flow rate. Figure 4A also shows that P0 is different for each Λ value, while it is similar for the SC and irregular

geometries. P0 is present but not discussed in other studies[7,22,34,37,38].

To identify which Λ value to select for a given geometry to obtain P0, we aim to redefine the discretization resolution (i.e., the X-axis in Figure 4A) such that it i) avoids using sphere diameter, and ii) accounts for the sample porosity. Our goal here is to extend the presented analysis beyond sphere packings of a given porosity to general porous media. Redefinition of the discretization resolution involves consideration of all meshes originating from the discretization of sphere packings as sets of voxels each with a known reference permeability value. For each mesh, dichotomy is used to find Λ^* matching the simulated permeability to the reference permeability. Next, we classify mesh voxels based on their type (`solid` or `fluid`), and the presence of neighbors of the same or opposite type. Voxel neighbors are identified using the connectivity of the selected lattice Boltzmann method with 18 horizontal and half-diagonal links in three dimensions. The `fluid`–`fluid` voxel class (FF) includes `fluid` type voxels without `solid` type neighbors, while the `fluid`–`solid` voxel class (FS) contains `fluid` type voxels with at least one `solid` neighbor each. The `solid`–`solid` (SS) and `solid`–`fluid` (SF) are classified with the same rule. Finally, to link Λ with χ at P0 we look for the dimensionless parameter χ for the X-axis in the following functional form:

$$\chi = \left(\frac{V_{\text{vox}}}{S_{\text{vox}}} \frac{\varepsilon_{\text{vox}}^a}{(1-\varepsilon_{\text{vox}})^b} \right)^c, \tag{1}$$

where a, b, c are some constants, $V_{\text{vox}}/S_{\text{vox}}$ is the voxel-based volume-to-surface ratio of solid or fluid phases, ε_{vox} is the voxel-based porosity, $\varepsilon_{\text{vox}}^a/(1-\varepsilon_{\text{vox}})^b$ is the factor entering, for example, the Kozeny–Carman equation[39]. Equation 1 is similar to the definition of hydraulic radius (e.g., eq. (42) in [20]). We vary constants a, b, c in steps of 1/2, allowing both positive and negative values. The proposed redefinition for χ is based on the volume-to-surface ratio of solid phase, has $a = 1$, $b = 0$, $c = 1/2$, and takes the following form:

$$\chi = \sqrt{\frac{\text{SS}}{\text{SF}} \frac{\text{FF}+\text{FS}}{\text{FF}+\text{FS}+\text{SF}+\text{SS}}} \tag{2}$$

which dimensionless in the voxelized representation. By contrast, the continuous analogue of equation (2) is dimensional and equals the square root of a characteristic length scale:

$$\sqrt{\frac{(\text{solid volume})}{(\text{solid surface})} \text{ porosity}}. \tag{3}$$

Figure 4B shows the grouping of Λ vs. χ pairs at P0 for all basic regular structures and a broad range of porosities (0.250–0.784), which provides the following linear correlation:

$$\Lambda^* = 0.27\chi + 0.043. \tag{4}$$

Please note that this linear correlation is obtained for the three basic regular packings: FCC, BCC, and SC. For completeness, we also add all periodic packings with the porosities of 0.2 and 0.15. Here, at lower resolutions we see a deviation of FCC packing from the general trend. These two porosities are omitted for the linear fit in Figure 4B.

VI. REDUCTION OF PERMEABILITY ERROR

We assess the accuracy of the linear correlation given by eq. (4) for irregular geometries using six irregular computer-generated packings and two laboratory-packed CT-scanned samples. This accuracy check is based on the parameter χ obtained for each voxelized geometry and running LBM flow simulations with Λ^* calculated according to eq. (4).

Computer-generated geometries include periodic irregular packings of mono- and poly-dispersed spheres as well as a packing confined laterally by the wall of a cylindrical container. The confining wall imposes partial ordering of sphere locations and introduces porosity and flow velocity maldistribution near the wall, propagating 3–5 diameters from the wall into the bulk (see Figures 2 and 4 in[40]). The impact of the confining wall is significant for the ratio of 10 sphere diameters per cylindrical container, and therefore this geometry is also used to assess eq. (4).

We also employed experimental geometries from our previous study[15] for evaluation of eq. (4). We packed two different types of commercially available glass beads, 0.47 mm beads1 and 0.54 mm beads2, in 8.98 mm and 9.04 mm glass tubes in water under ultrasonic vibration (Appendix A in[15]), resulting in samples P3 and P4, and determined their permeability experimentally. Hereafter, both samples were scanned using CoreTOM X-Ray CT scanner (XRE Tescan, Ghent, Belgium) using the tube voltage of 60 kV and power of 15W. Each sample was scanned at 18 resolutions. The number of two-dimensional (2D) projections ranged from 250 to 1800, while the exposure to obtain each projection was about 4.5s, Appendix B1 in[15]. Gray CT images were segmented using global thresholds each equal to the laboratory-determined porosity values. Simulated permeability for samples P3 and P4 agrees with experimental values within 1%. The reference dimensionless permeability (porosity) value for P3 is 5.82×10^{-4} (0.354) while for P4 is 6.02×10^{-4} (0.355), see Appendices A3 and C3 in[15]. More details on the preparation and experimental measurements for samples P3 and P4, their imaging, image processing, and simulations are provided in[15]. All 3D images[41],

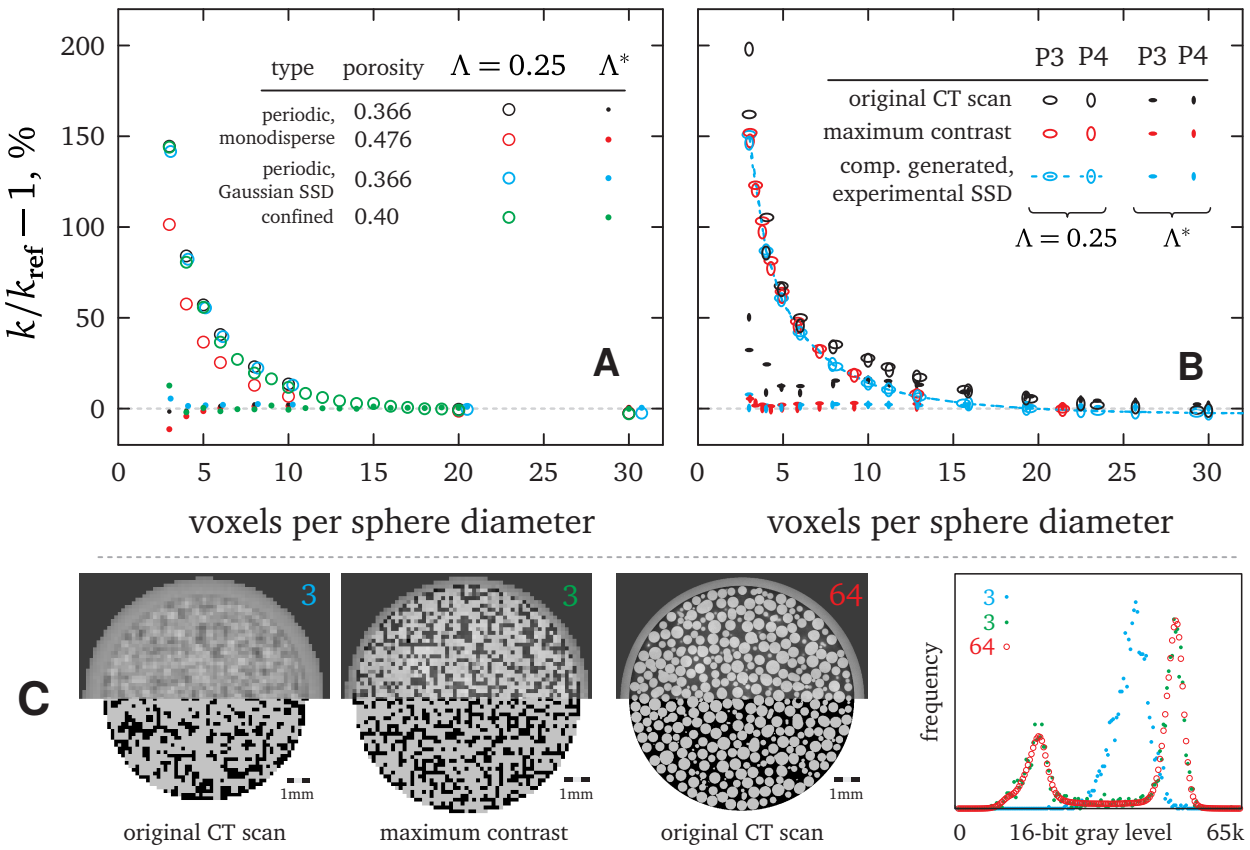

FIG. 5. A,B: Relative error in permeability for 10 computer-generated and CT-scanned geometries. Flow simulations are performed with $\Lambda = 0.25$ and Λ^* from eq. (4). C: Slices of gray and segmented 3D images of the CT-scanned sample P3 (0.47 mm glass beads inside a 9 mm glass tube[15]). Image resolutions are 3 and 64 voxels per Sauter sphere diameter. C, right panel: the corresponding gray level distributions. See Figure 9 for an extended version of panel C, which also includes sample P4.

2D CT projections[42], and 2D optical scans of beads1 and beads2 with experimental logs[43] are available online.

Sphere size distributions (SSD) obtained from 2D optical scans of beads1 and beads2 were used to computer-generate irregular periodic packings at porosity of 0.362 (Figure 24 in[15]). Extrapolating from the LBM simulations with $\Lambda = 0.05$[24], we determined the reference 0.1%-accurate permeability values for computer-generated packings as 6.851×10^{-4} for beads1 SSD and 6.833×10^{-4} for beads2 SSD, see Table II.

To benchmark the accuracy of eq. (4) on CT images of real objects, we need to consider the impact of image contrast. X-ray computed-tomography scanning produces images with a reduced contrast (blue "3" panel in Figure 5C) in comparison to computer-generated and

discretized geometries, which have no contrast loss. Recent research[15] has demonstrated that at lower resolutions the contrast of CT images affects the simulated permeability. This was observed using an operator-independent global segmentation procedure of gray CT images, based on the laboratory-measured porosity. The images with maximum contrast (e.g., green "3" in Figure 5C) were obtained by downsampling high-resolution CT images (similar to "64" in Figure 5C), see Appendix B2 in[15]. The same study observed that for these maximum-contrast images the error in permeability is identical to the computer-generated geometries, Figures 2 and 27A,B in [15]. Therefore, we use the images of maximum contrast from the earlier study[15] to simulate flow with Λ^* from eq. (4). These downsampled, maximum contrast images are available online[41].

Figure 5A,B shows a comparison of the simulated permeabilities obtained in the current study using a common value of $\Lambda = 0.25$ (equivalent to $\tau = 1$ for BGK collision operator) and Λ^* from (4). For all geometries, the proposed correlation (4) brings the permeability error to unexpectedly low levels, as seen in Figure 5A,B. Our results demonstrate that selection of Λ^* according to eq. (4) enables accurate simulation results from unresolved, highly-voxelized images.

Decrease of the discretization resolution in flow simulations allows to save computational time significantly: the computational complexity of the employed LBM simulation approach scales as $O(\text{resolution}^5)$ meaning that computational time between resolutions 4 and 64 differ $O(16^5) \approx O(10^6)$ times. Despite more efficient finite difference solvers for Stokes PDE are available[44] (although at a cost of a higher discretization errors due to the reduced voxel connectivity), the computational efforts will still grow rapidly with the resolution increase. Also, reducing the resolution saves CT scanning time: according to our experience, scanning a sample at the resolution of 4 voxels per sphere diameter takes about 10 minutes while the resolution of 64 voxels requires 1200 minutes. Alternatively, reduction of the CT resolution allows to scan larger volumes of the sample at a fixed scanning time.

VII. CONCLUSION

To date, efforts to improve the simulation accuracy of flow through porous media have targeted localization of pore surfaces of original, non-discretized geometries[18,32,45]. During imaging of a real porous medium, scanning equipment maps the porous medium geometry onto a discrete uniform mesh. Superposition of the real geometry and the mesh results in

the formation of a superstructure (Figures 1 and 3). The existence of this superstructure suggests that relying on pore surfaces (within one unit cell or a representative volume) is fundamentally limited with decreases in resolution to low values. This limitation originates from the incomplete information about the pore space geometry and the corresponding flow field at the unit cell level. At each low resolution, the superstructure corresponding to this resolution and geometry controls flow. More generally, superstructures control not only flow but also morphological and topological information about a given geometry. Superstructures also prevent pore-level analysis from producing the optimal magic number, Λ. By contrast, increases in resolution from low to high values result in both the recovery of pores and the flow through the image of the original, non-discretized geometry (Figure 8).

Currently, performing accurate simulations of pore-scale flows demands an accurate, visually appealing representation of the pore space (red "64" panel in Figure 5C). Reduction of the mesh resolution to a few voxels per pore results in a pore space that is highly voxelated and unattractive to the human eye (blue, red "3" panels in Figure 5C). However, we show that flow simulations on these highly-voxelated images can accurately reproduce the experimental permeability (i.e., the flow physics) because of the existence of superstructures, which retain information about the pore space over scales significantly exceeding a single pore dimension or representative volume of a porous sample.

The geometrical origin of the superstructures indicates that the presented findings are not limited to a particular numerical method (here LBM, see also Figure 7 for the finite difference flow fields) or to a particular flow problem (Stokes flow). As mentioned previously[25], variation of Λ in LBM simulations is similar to, e.g., a finite difference method, in which the derivative coefficients can be adjusted. Such adjustment changes the order of convergence of the method, as well as its error magnitude. Here one should keep in mind that for the final simulation results the error magnitude is of key importance rather than its convergence rate.

The correlation (4) identifies the free magic parameter Λ such that the individual error contributions (bulk and boundary errors of the numerical scheme and integration error in calculating the average flow rate) of potentially opposite signs cancel each other out. This formal approach can be applied to other phenomena simulated by numerical solutions of PDEs. As we see it, the key ingredients to successfully implement our approach are: a discrete uniform mesh, numerical scheme (here LBM), existence of the null point where the

error is zero, and a target integral quantity (here permeability). We expect that the error cancellation can be achieved not only by the spatial replication of a target object (here a unit cell) to obtain a superstructure, but also by the object's behavior in time (e.g., when the object or its features move). Thus, the presented approach can be used for better positioning of arrays of sensors, improved temporal measurements, or better quantification of pixelized images provided, for example, by drones or satellites.

Author Declarations. The authors have no conflicts to disclose. The data that support the findings of this study are available from the corresponding author upon reasonable request.

ACKNOWLEDGMENTS

We are grateful for the allocation of computational resources by the Supercomputing Laboratory at King Abdullah University of Science and Technology (KAUST) in Thuwal, Saudi Arabia. We are thankful to Gabrielle E. Abelskamp for her editorial support. We thank the anonymous reviewers of JFM-2024-1620 submission for their helpful comments. *Funding:* This work was supported through funding to the Ali Al-Naimi Petroleum Engineering Research Center (ANPERC) at KAUST. *Contributions*: S. K. suggested the existence of discrete superstructures, introduced the concept of null point, wrote manuscript draft, and prepared figures. T. P. organized and supported this research, supervised it and edited the paper. S. K. introduced the fractional discretization in the joint study with Dr. Irina Ginzburg (10.1016/j.jcp.2014.10.038) after I. G. suggestion to preserve symmetry of the analytical geometry during discretization.

REFERENCES

[1]R. J. Hill, D. L. Koch, and A. J. C. Ladd, "The first effects of fluid inertia on flows in ordered and random arrays of spheres," Journal of Fluid Mechanics **448**, 213–241 (2001).

[2]G. Guiochon, "Monolithic columns in high-performance liquid chromatography," Journal of Chromatography A **1168**, 101–168 (2007).

[3]A.-R. Khaled and K. Vafai, "The role of porous media in modeling flow and heat transfer in biological tissues," International Journal of Heat and Mass Transfer **46**, 4989–5003 (2003).

[4]A. D. Khawaji, I. K. Kutubkhanah, and J.-M. Wie, "Advances in seawater desalination technologies," Desalination **221**, 47–69 (2008).

[5]A. Nommeots-Nomm, C. Ligorio, A. Bodey, B. Cai, J. Jones, P. Lee, and G. Poologasundarampillai, "Four-dimensional imaging and quantification of viscous flow sintering within a 3D printed bioactive glass scaffold using synchrotron X-ray tomography," Materials Today Advances **2**, 100011 (2019).

[6]R. K. Jain, J. D. Martin, and T. Stylianopoulos, "The role of mechanical forces in tumor growth and therapy," in *Annual Review of Biomedical Engineering*, Vol. 16, edited by M. L. Yarmush (2014) pp. 321–346.

[7]C. Manwart, U. Aaltosalmi, A. Koponen, R. Hilfer, and J. Timonen, "Lattice-boltzmann and finite-difference simulations for the permeability for three-dimensional porous media," Phys. Rev. E **66**, 016702 (2002).

[8]S. S. Kohles, J. B. Roberts, M. L. Upton, C. G. Wilson, L. J. Bonassar, and A. L. Schlichting, "Direct perfusion measurements of cancellous bone anisotropic permeability," Journal of Biomechanics **34**, 1197–1202 (2001).

[9]M. F. Lagadec, R. Zahn, and V. Wood, "Characterization and performance evaluation of lithium-ion battery separators," Nature Energy **4**, 16–25 (2019).

[10]M. Josh, L. Esteban, C. Delle Piane, J. Sarout, D. N. Dewhurst, and M. B. Clennell, "Laboratory characterisation of shale properties," Journal of Petroleum Science and Engineering **88–89**, 107–124 (2012).

[11]P. Shrestha and B. Stoeber, "Imaging fluid injections into soft biological tissue to extract permeability model parameters," Physics of Fluids **32**, 011905 (2020).

[12]S. Modha, C. Castro, and H. Tsutsui, "Recent developments in flow modeling and fluid control for paper-based microfluidic biosensors," Biosensors and Bioelectronics **178**, 113026 (2021).

[13]D. Maggiolo and S. Sasic, "Respiratory droplets interception in fibrous porous media," Physics of Fluids **33**, 083305 (2021).

[14]S. K. Mohammadian, S. M. Rassoulinejad-Mousavi, and Y. Zhang, "Thermal management improvement of an air-cooled high-power lithium-ion battery by embedding metal foam," Journal of Power Sources **296**, 305–313 (2015).

[15]S. Khirevich, M. Yutkin, and T. Patzek, "Correct estimation of permeability using experiment and simulation," Physics of Fluids **34**, 123603 (2022).

[16]M. A. V. D. Hoef, R. Beetstra, and J. A. M. Kuipers, "Lattice-boltzmann simulations of low-reynolds-number flow past mono- and bidisperse arrays of spheres: results for the permeability and drag force," Journal of Fluid Mechanics **528**, 233–254 (2005).

[17]C. Pan, L.-S. Luo, and C. T. Miller, "An evaluation of lattice Boltzmann schemes for porous medium flow simulation," Comput. Fluids **35**, 898–909 (2006).

[18]G. Silva and I. Ginzburg, "Reviving the local second-order boundary approach within the two-relaxation-time lattice boltzmann modelling," Philosophical Transactions of the Royal Society A: Mathematical, Physical and Engineering Sciences **378**, 20190404 (2020).

[19]M. V. Karsanina, K. M. Gerke, E. B. Skvortsova, A. L. Ivanov, and D. Mallants, "Enhancing image resolution of soils by stochastic multiscale image fusion," Geoderma **314**, 138–145 (2018).

[20]S. Whitaker, "Forced convection heat transfer correlations for flow in pipes, past flat plates, single cylinders, single spheres, and for flow in packed beds and tube bundles," AIChE Journal **18**, 361–371 (1972).

[21]Y. Cengel and J. Cimbala, *Fluid Mechanics Fundamentals and Applications*, 3rd ed. (McGraw-Hill, 2013).

[22]S. Khirevich, I. Ginzburg, and U. Tallarek, "Coarse- and fine-grid numerical behavior of MRT/TRT lattice-Boltzmann schemes in regular and random sphere packings," Journal of Computational Physics **281**, 708–742 (2015).

[23]I. Ginzburg, F. Verhaeghe, and D. d'Humieres, "Two-relaxation-time Lattice Boltzmann scheme: About parametrization, velocity, pressure and mixed boundary conditions," Communications in Computational Physics **3**, 427–478 (2008).

[24]S. Khirevich and T. W. Patzek, "Behavior of numerical error in pore-scale lattice boltzmann simulations with simple bounce-back rule: Analysis and highly accurate extrapolation," Physics of Fluids **30**, 093604 (2018).

[25]D. d'Humieres and I. Ginzburg, "Viscosity independent numerical errors for Lattice Boltzmann models: From recurrence equations to "magic" collision numbers," Computers & Mathematics with Applications **58**, 823–840 (2009).

[26]Y. H. Qian, D. d'Humieres, and P. Lallemand, "Lattice bgk models for navier-stokes equation," Europhysics Letters **17**, 479–484 (1992).

[27]D. d'Humières, "Generalized lattice Boltzmann equations Rarefied Gas Dynamics: Theory and Simulations," Prog. Astronaut. Aeronaut. **159**, 450–458 (1992).

[28]M. Geier, M. Schönherr, A. Pasquali, and M. Krafczyk, "The cumulant lattice boltzmann equation in three dimensions: Theory and validation," Computers & Mathematics with Applications **70**, 507–547 (2015).

[29]P. Lallemand and D. d'Humières, "Numerical simulations of hydrodynamics with lattice gas automata in two dimensions," Complex Systems **1**, 599–632 (1987).

[30]M. Rohde, D. Kandhai, J. J. Derksen, and H. E. A. Van den Akker, "Improved bounce-back methods for no-slip walls in lattice-boltzmann schemes: Theory and simulations," Physical Review E **67**, 066703 (2003).

[31]D. d'Humières, I. Ginzburg, M. Krafczyk, P. Lallemand, and L.-S. Luo, "Multiple-relaxation-time lattice boltzmann models in three dimensions," Philosophical Transactions of the Royal Society of London. Series A: Mathematical, Physical and Engineering Sciences **360**, 437–451 (2002).

[32]X. Yang, Y. Mehmani, W. A. Perkins, A. Pasquali, M. Schönherr, K. Kim, M. Perego, M. L. Parks, N. Trask, M. T. Balhoff, M. C. Richmond, M. Geier, M. Krafczyk, L.-S. Luo, A. M. Tartakovsky, and T. D. Scheibe, "Intercomparison of 3d pore-scale flow and solute transport simulation methods," Advances in Water Resources **95**, 176–189 (2016).

[33]I. Ginzbourg and P. M. Adler, "Boundary flow condition analysis for the three-dimensional lattice boltzmann model," J. Phys. II France **4**, 191–214 (1994).

[34]L. Talon, D. Bauer, N. Gland, S. Youssef, H. Auradou, and I. Ginzburg, "Assessment of the two relaxation time Lattice-Boltzmann scheme to simulate Stokes flow in porous media," Water Resources Research **48**, W04526 (2012).

[35]W. E. Lorensen and H. E. Cline, "Marching cubes: A high resolution 3d surface construction algorithm," in *Proceedings of the 14th Annual Conference on Computer Graphics and Interactive Techniques*, SIGGRAPH '87 (Association for Computing Machinery, New York, NY, USA, 1987) pp. 163–169.

[36]E. Dalla, M. Hilpert, and C. T. Miller, "Computation of the interfacial area for two-fluid porous medium systems," Journal of Contaminant Hydrology **56**, 25–48 (2002).

[37]R. Verberg and A. Ladd, "Accuracy and stability of a lattice-boltzmann model with subgrid scale boundary conditions," Physical Review E **65** (2002), 10.1103/PhysRevE.65.016701.

[38]Y. Han and P. A. Cundall, "Lattice boltzmann modeling of pore-scale fluid flow through idealized porous media," International Journal for Numerical Methods in Fluids **67**, 1720–1734 (2011).

[39]F. Dullien, ed., *Porous Media: Fluid Transport and Pore Structure*, 2nd ed. (Academic Press, San Diego, 1992).

[40]S. Khirevich, A. Holtzel, D. Hlushkou, and U. Tallarek, "Impact of conduit geometry and bed porosity on flow and dispersion in noncylindrical sphere packings," Analytical Chemistry **79**, 9340–9349 (2007).

[41]S. Khirevich, M. Yutkin, and T. W. Patzek, "3D X-ray computed tomography images of packed glass beads scanned at 18 resolutions (gray and segmented, with simulated permeability values). https://doi.org/10.25452/figshare.plus.16821412," (2022).

[42]S. Khirevich, M. Yutkin, and T. W. Patzek, "3D X-ray computed tomography images of packed glass beads scanned at 18 resolutions (2D projections and 3D gray reconstructions). https://doi.org/10.25452/figshare.plus.16850653," (2022), 10.25452/figshare.plus.16850653.

[43]S. Khirevich, M. Yutkin, and T. W. Patzek, "Pressure and viscosity logs for permeability estimation of P3 and P4 samples. Experimental permeability values. 2D optical scans of beads1 and beads2. https://doi.org/10.25452/figshare.plus.16867417," (2022), 10.25452/figshare.plus.16867417.

[44]N. M. Evstigneev, O. I. Ryabkov, and K. M. Gerke, "Stationary stokes solver for single-phase flow in porous media: A blastingly fast solution based on algebraic multigrid method using gpu," Advances in Water Resources **171**, 104340 (2023).

[45]M. Bouzidi, M. Firdaouss, and P. Lallemand, "Momentum transfer of a Boltzmann-lattice fluid with boundaries," Physics of Fluids **13**, 3452–3459 (2001).

[46]R. E. Larson and J. J. L. Higdon, "A periodic grain consolidation model of porous media," Phys. Fluids **38**, 38–46 (1989).

[47]S. Khirevich and T. W. Patzek, "Comment on "A periodic grain consolidation model of porous media" [Phys. Fluids A 1, 38 (1989)]," Physics of Fluids **31** (2019), 10.1063/1.5116700.

[48]K. M. Gerke, R. V. Vasilyev, S. Khirevich, D. Collins, M. V. Karsanina, T. O. Sizonenko, D. V. Korost, S. Lamontagne, and D. Mallants, "Finite-difference method stokes solver (fdmss) for 3d pore geometries: Software development, validation and case studies," Computers & Geosciences **114**, 41–58 (2018).

Appendix A: Reference permeability values

porosity	FCC	BCC	SC
0.250	$\mathbf{1.54 \cdot 10^{-4}}$	$\mathbf{2.46 \cdot 10^{-4}}$	$\mathbf{2.98 \cdot 10^{-4}}$
0.366	$5.98 \cdot 10^{-4}$	$7.66 \cdot 10^{-4}$	$\mathbf{1.03 \cdot 10^{-3}}$
0.476	$1.85 \cdot 10^{-3}$	$2.05 \cdot 10^{-3}$	$2.52 \cdot 10^{-3}$
0.784	$3.32 \cdot 10^{-2}$	$3.32 \cdot 10^{-2}$	$3.46 \cdot 10^{-2}$
0.150	$\mathbf{2.89 \cdot 10^{-5}}$	$\mathbf{5.84 \cdot 10^{-5}}$	$\mathbf{5.33 \cdot 10^{-5}}$
0.200	$\mathbf{7.55 \cdot 10^{-5}}$	$\mathbf{1.31 \cdot 10^{-4}}$	$\mathbf{1.43 \cdot 10^{-4}}$

TABLE I: Reference dimensionless permeability values for regular geometries at indicated porosities. The permeability values are normalized by sphere diameter squared and obtained using extrapolation with $\Lambda = 0.05$[24]. **Bold** typeface highlights the permeability for geometries with overlapping spheres. These values differ from the previously reported values of[46] as explained in[47].

geometry	porosity	reference permeability
irregular periodic	0.366	$7.14 \cdot 10^{-4}$
irregular periodic	0.476	$2.39 \cdot 10^{-3}$
irregular periodic, SSD	0.366	$7.15 \cdot 10^{-4}$
irregular confined	0.400	$9.06 \cdot 10^{-4}$
irregular, SSD (beads1)	0.3624	$6.85 \cdot 10^{-4}$
irregular, SSD (beads2)	0.3626	$6.83 \cdot 10^{-4}$
lab. prepared, P3 (beads1)	0.3544	$5.82 \cdot 10^{-4}$
lab. prepared, P4 (beads2)	0.3552	$6.03 \cdot 10^{-4}$

TABLE II: Reference dimensionless permeability values for irregular geometries at indicated porosities obtained using extrapolation with $\Lambda = 0.05$[24]. The permeability values are normalized by sphere diameter squared or Sauter sphere diameter squared, where applicable.

Appendix B: Additional figures

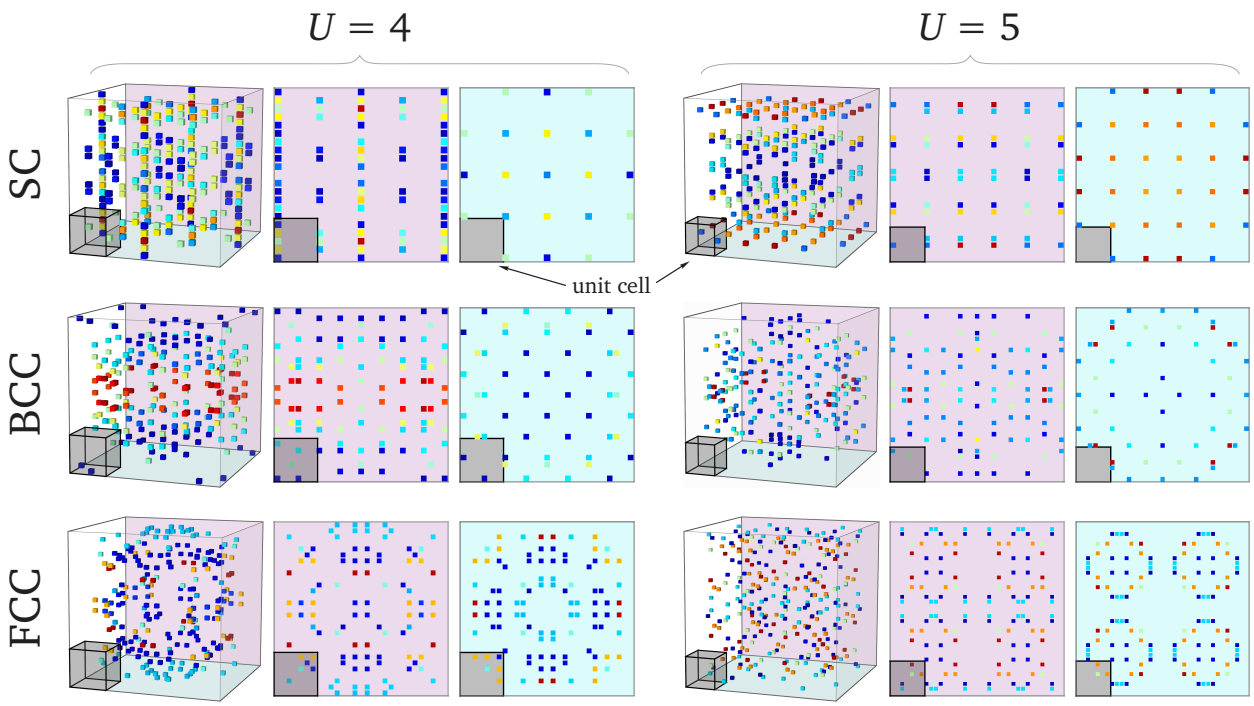

	SC	BCC	FCC
$v^*_{\min}$	2.54	2.06	2.19
$v^*_{\max}$	4.06	2.57	2.86
L^3	21^3	25^3	29^3
number of voxels	210	210	235

$U = 4$

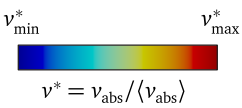

	SC	BCC	FCC
$v^*_{\min}$	3.18	2.18	2.25
$v^*_{\max}$	3.86	2.76	3.21
L^3	26^3	31^3	36^3
number of voxels	210	210	276

$U = 5$

FIG. 6. Extension of Figure 3 for the cases of $U = 4$ and $U = 5$, where each panel displays approximately 200 voxels with the highest absolute velocity magnitude extracted from the full velocity field for SC, BCC, and FCC geometries of touching spheres. Discretization resolution is about 5.3 voxels per sphere diameter for all geometries.

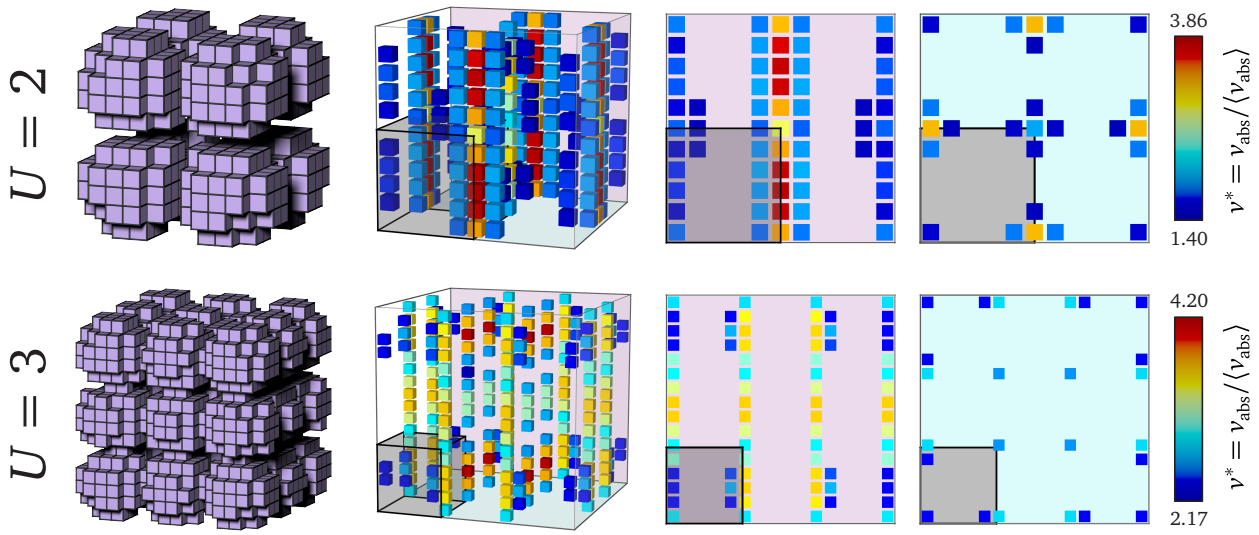

FIG. 7. Finite difference simulations of flow in SC geometry with $U = 2$ and $U = 3$ using open-source FDMSS package[48]. Discrete superstructures are also visible similar to Figure 3. Flow fields obtained with FDMSS differ from LBM flow fields due to the difference in voxel connectivity of FDMSS (6-voxel) and LBM (18-voxel).

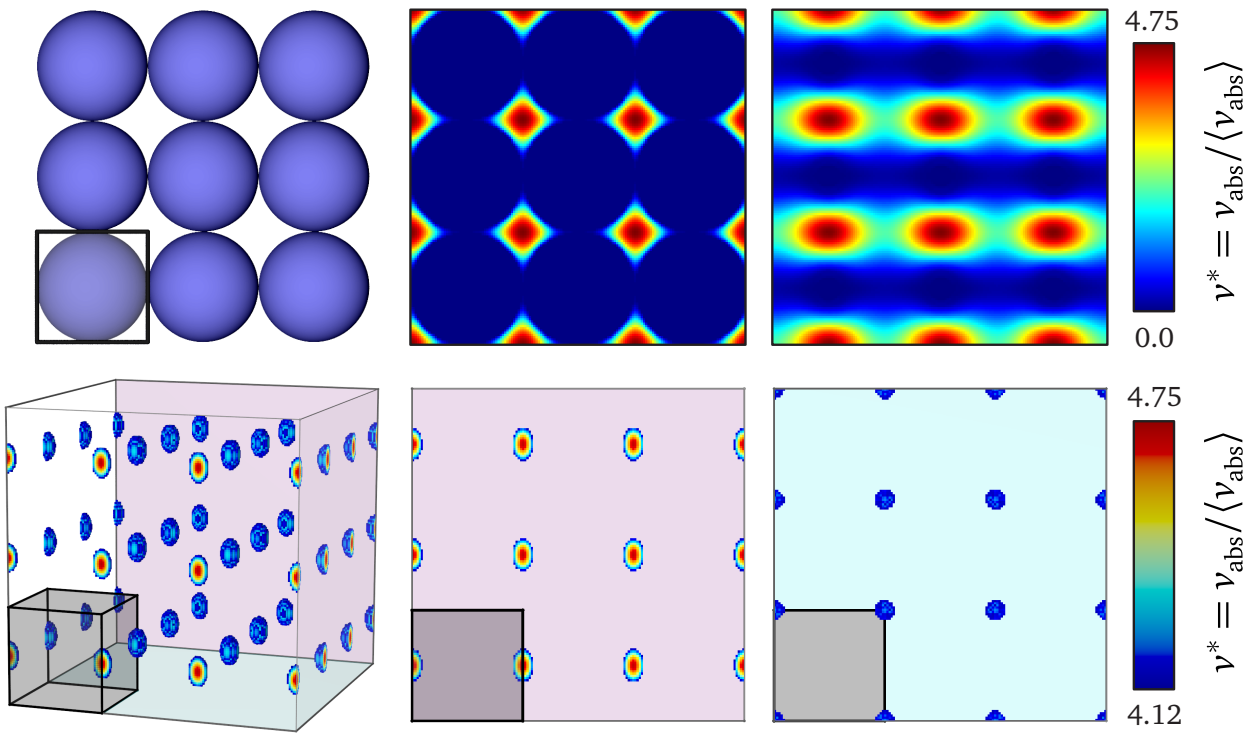

FIG. 8. High-resolution flow simulation of flow in SC geometry. Simulation domain dimensions are 151^3 and $U = 3$, resulting in the discretization resolution of about 50 voxels per diameter. Top row: analytical geometry, slices of the 3D absolute velocity field at $Z = 26$ (middle) and $Y = 1$ (right). Bottom row: top 1% of voxels with the largest absolute velocity. As expected, the flow field pattern repeats the periodic geometry.

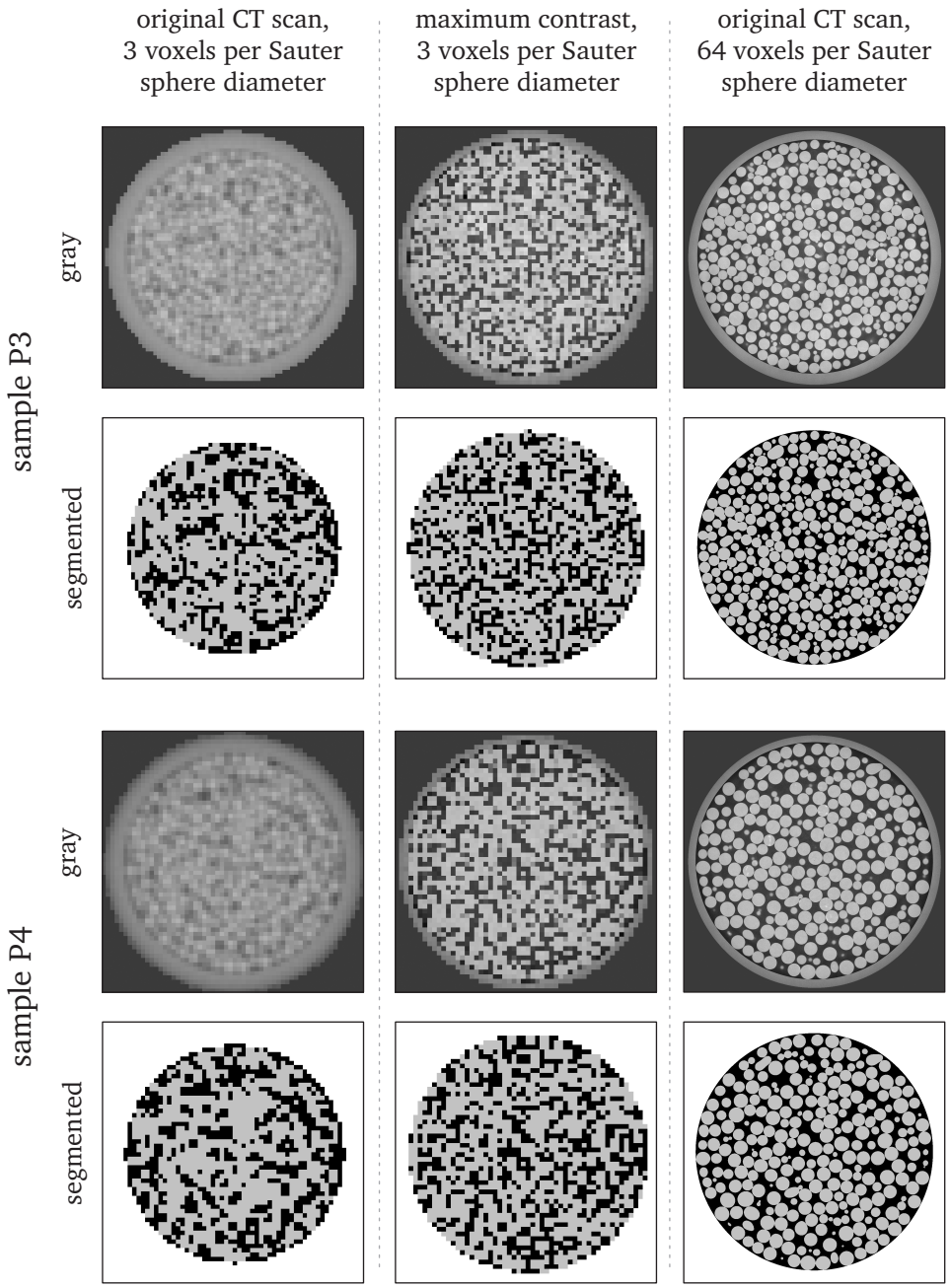

FIG. 9. An extended view of panel C in Figure 5. The displayed gray CT images and the segmented images are for the samples P3 and P4[15]. Estimated diameters of the confining glass tube are 8.98 mm and 9.04 mm for P3 and P4 samples, respectively. When viewing this figure as `pdf`, please zoom each panel significantly (1000+%) to avoid image distortion due to the on-screen interpolation. Full gray and segmented 3D images are available online in the corresponding dataset[41].